

# Design optimization of a lightweight rocker–bogie rover for ocean worlds applications

Hari Nayar<sup>1</sup> , Junggon Kim<sup>1</sup>, Brendan Chamberlain-Simon<sup>1</sup>,  
Kalind Carpenter<sup>1</sup>, Michael Hans<sup>1</sup>, Anna Boettcher<sup>1</sup>,  
Gareth Meirion-Griffith<sup>1</sup>, Brian Wilcox<sup>1</sup> and Brian Bittner<sup>2</sup>

## Abstract

Relatively recent discoveries have shown that large quantities of water can be found on moons of some of the planets among the gas giants in our solar system. Robotic mobility systems can study the varied geology and origins of these bodies if they are able to navigate the complex terrains of ocean worlds. The topographical features of ocean worlds present a unique combination of challenges for mobility. These include cryogenic ice, penitentes, salt evaporites, chaotic regions, and regolith with uncertain shear and sinkage properties. Uncertainty in both terrain properties and geometry motivates design of a platform that is mobile within a large range of obstacle geometries and terrain properties. This article reports on a research effort to study the requirements and numerically optimize the kinematic parameters of the rover to satisfy these goals. The platforms selected in the process were further verified via simulation. A simulation and analysis of grouser generated suitable designs for interaction with similar ledges and rough terrain. From this analysis, a prototype was developed and tested to meet the wide range of topography and terramechanics conditions expected on these bodies.

## Keywords

Planetary surface exploration, ocean worlds, rocker–bogie rover, wheeled mobility, mobility optimization

Date received: 30 July 2019; accepted: 23 September 2019

Topic: Mobile Robots and Multi-Robot Systems

Topic Editor: Nak-Young Chong

Associate Editor: Chang-bae Moon

## Introduction

Discovery of large quantities of water among bodies in our outer solar system has boosted interest in future space missions to these bodies.<sup>1,2</sup> The ingredients for life,<sup>3</sup> (1) liquid water, (2) rocky cores in contact with the oceans to provide salts and other chemicals needed for life, (3) energy fed into the oceans either from hydrothermal sources in the mantle or tidal activity, and (4) stable environments that could promote production of complex molecules and potentially life, are all likely on Europa, a moon of Jupiter, and Enceladus, a moon of Saturn.

One of the principle goals for missions to these ocean world bodies is to gather astrobiological data. Finding life

or signs of life beyond earth would be an extraordinary discovery. More easily attainable goals of understanding the geology and origins of ocean worlds are also of a significant science value.<sup>4</sup> Evidence from previous missions and remote sensing from earth shows that Europa and

<sup>1</sup>Robotics and Mobility Systems, California Institute of Technology, NASA Jet Propulsion Laboratory, Pasadena, USA

<sup>2</sup>Robotics Institute, University of Michigan, Ann Arbor, USA

### Corresponding author:

Hari Nayar, Robotics and Mobility Systems, California Institute of Technology, NASA Jet Propulsion Laboratory, Pasadena, CA 91101, USA.  
Email: hdnayar@jpl.nasa.gov



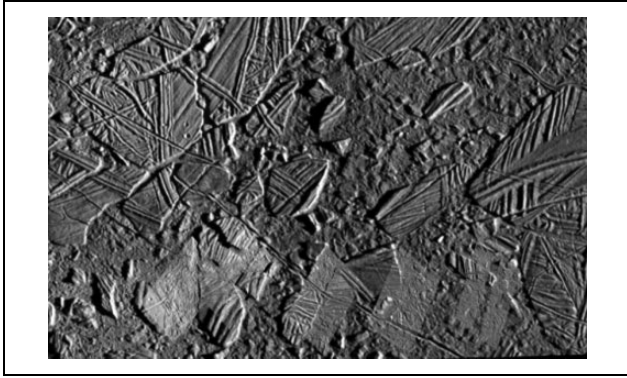


**Figure 1.** Mosaic of Conamara Chaos region on Europa. Image credit: NASA/JPL/U Arizona.

Enceladus both have varied and active or recently active surface geologic processes.<sup>5</sup> A mission to explore a large range of terrain types would provide an understanding of the origins and history of the body.

A study was conducted to generate robotic surface mobility concepts to cover a large range of the surface of ocean world bodies. The requirements for the concepts were to (1) be able to cover a distance of at least 10 km over a range of terrain types to be found on ocean worlds, (2) handle the range of material types from hard ice rock to noncohesive granular ice, and (3) operate in the environmental conditions of cryogenic temperatures and vacuum and meet mission constraints of power, mass, and volume. The 10 km drive goal was derived from a study of images of Europa, for example, as shown in Figure 1, showing a 35 km by 50 km patch of varied terrain, where it was determined that, with an appropriately selected landing site, it would be possible to visit at least three different terrain types within a 10-km travel distance. Among the concepts generated was a vehicle that drives over the surface. Earlier results from this work were reported in Nayar et al.<sup>6</sup> This article provides more details and includes an analysis of wheel grousers and experimental and field results from tests conducted on the prototype vehicle.

The contributions of this article are multifold. First, the known geological features of ocean worlds are organized and presented as potential mobility hazards. This information is immediately useful for the design and development of systems to be sent to regions with similar mechanical and topographical properties. Next, the motivation for the design is provided. The design kinematics are optimized via simulation using metrics that prioritize the extreme nature of ocean world terrains. A subsequent simulation-based analysis identified ranges of grouser designs that interact with ledges and identified parameters for the extreme geometric obstacles. Experimental validation of a prototype confirms the viability of the platform optimized through analysis and simulation.

The article begins with a survey of terrain classes on Europa and their relation to mobility (second section).

These considerations drive three design requirements for the mobile platform (third section). The subsequent kinematic optimization framework (fourth section) is evaluated via simulation (fifth section). Given platform kinematics, a study of grousers renders a design space of suitable wheels (sixth section). A prototype was built using the recommended design parameters from the analysis and simulation. The performance of the prototype was compared to the predicted performance (seventh section). The article concludes with a summary (eighth section). The overall development process pursued in this study is illustrated in Figure 2.

## Environmental considerations

Water is an essential ingredient for life. Recent observations in the outer solar system have revealed that many satellites of the outer planets contain large quantities of water. These bodies, along with our earth, have been called ocean worlds. Europa and Enceladus are of particular interest and prime targets because of the confirmed presence of liquid water below their icy crusts. Liquid water also implies that they have a subsurface energy source, another essential ingredient for life. In addition to the astrobiology goal, surface exploration has science value for studies of ice geology and planetary origins. The environmental conditions for mobility on these bodies are challenging. The surface temperature on Europa is between 76 K and 130 K,<sup>7</sup> while on Enceladus, it is between 65 K and 140 K.<sup>8</sup> Europa poses the additional burden of designing for high radiation exposure at its surface.<sup>9</sup> The greatest challenge is possibly the surface topography and mechanical properties of the terrain. The ice crusts covering Europa and Enceladus are primarily composed of water many kilometers thick. The Cassini and Galileo missions have, respectively, shown distinct surface features that include double ridges, bands, chaos, and lenticulae. Surface mobility will be challenging over the varied and rugged terrain. Furthermore, plume vents have been detected on Enceladus by Cassini<sup>1</sup> and more recently on Europa by Hubble.<sup>10</sup> Deposition of condensate from the plumes on the surface in proximity to the vents will probably be fine-grained cryogenic ice regolith, posing another challenge for surface mobility.

This study focuses on the vehicle design to address the topography and terramechanics. For the deployment on an ocean world body, additional measures will have to be taken. For example, to meet the constraints of temperature extremes, designs using heaters to maintain temperatures within the operating ranges of component systems or using components that can withstand the extreme low temperature or a combination are possible. A myriad of other precautions, for example, shielding against radiation on Europa, will be needed for the cruise to, descent, landing and operation on the surface.

The gravitational field at the surface on Europa is  $1.3 \text{ m/s}^2$  (slightly lower than our moon's gravitational

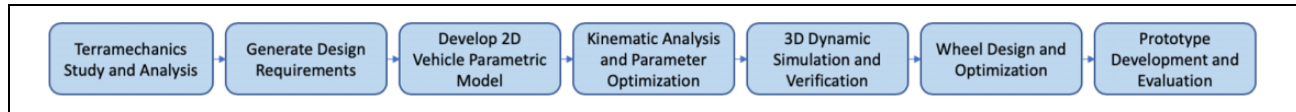


**Figure 2.** The steps in the development process taken in this study.

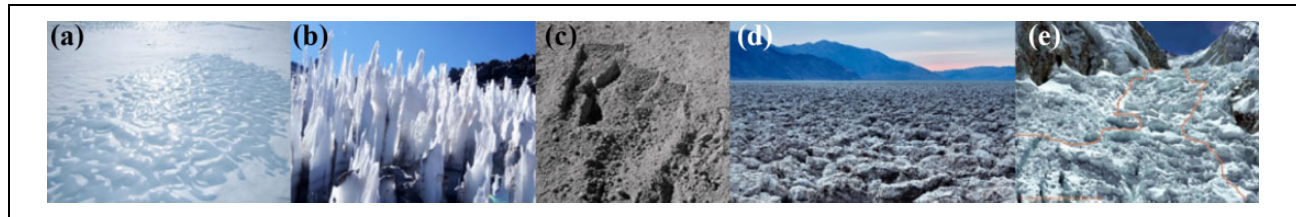


**Figure 3.** From left to right: (a) cryogenic ice, (b) penitentes, (c) regolith, (d) salt evaporites, and (e) chaos.

strength) while on Enceladus it is  $0.11 \text{ m/s}^2$ . This large difference will require significantly different strategies for dynamic driving over the surface. It may even be possible to take advantage of the very low gravity on Enceladus and use modes of traverse that liftoff over the surface. The quasi-static analysis for vehicle design, however, is still applicable as the vehicle would be driven in slow and precise motions on the surface during science operations.

The design of vehicles to traverse over these bodies requires knowledge about the topography and mechanical properties of the surface. These are both strategies being pursued in the development of future surface mission systems. The highest resolution surface imagery we currently have are from Galileo (orbiting Jupiter) and Cassini (orbiting Saturn) with pixel sizes of 6 m and 20 m, respectively. These resolutions are significantly larger than likely vehicle sizes and do not provide adequate information of the surface at the vehicle scale. Earth analog studies have identified several pathological cases that need to be considered for robotic mobility. They include cryogenic ice, penitentes, regolith, salt evaporites, and chaos terrain, as illustrated in Figure 3. These are described in the following subsections. To better understand the mechanical properties of material on the surface, samples were tested under cryogenic and vacuum conditions. The results are also reported in a following subsection.

### Cryogenic ice

The near-surface material on Europa and Enceladus is primarily composed of cryogenic ice (Figure 3(a)). Unlike naturally occurring ice on the surface of the earth, cryogenic ice is exceptionally hard, with a compressive strength measured at 110–120 MPa in laboratory tests.<sup>11</sup> It can take on many morphologies (Figure 3(b), (c), and (e)) as described in the following subsections.

### Penitentes

At low surface pressures (as is the case on Europa and Enceladus), and incident solar illumination close to perpendicular (at equatorial latitudes), near-vertical ice spikes up to 1–5 m in length, called penitentes, form naturally (Figure 3(b)) due to solar concentration and ice sublimation in troughs.<sup>12</sup> On earth, these are observed in the Andes. Mobility over penitentes is difficult to conceive and will probably require a specialized mobility system to handle their unique morphology.

### Cryogenic ice regolith

The presence of an ice regolith and measurement of the characteristics of the top layer of ice have been derived from remote sensing. Estimates of ice particle sizes in the range of twenty to several hundreds of micrometers in size are predicted from photometry in the visible spectrum range of 380–770 nm. At these wavelengths, light penetrates only the top tens of micrometers<sup>13</sup> of the surface, but these observations may imply significant depths of material with these properties. Surface compaction and void ratios in the surface material have been measured at 25% on the leading side of Europa and 75% on the trailing side.<sup>14</sup> These are consistent with expected values due to the variation of surface exposure to radiation on the leading and trailing sides. In addition, the upper most layer of the surface is likely formed of  $<1.5 \mu\text{m}$  particles with void spaces of up to 95% or more.<sup>13,15</sup> RADAR measurements<sup>16</sup> show that both Europa and Enceladus are bright to backscatter at a wide range of wavelengths implying likelihood of a very well-graded regolith that may be many meters deep.

### Salt evaporites

Remote sensing imagery showing brown, orange, or yellow surface discolorations on the surface of Europa is believed to indicate salt evaporites (Figure 3(d)) composed of

non-ice chemical species deposited on the surface either from subsurface materials or from material deposited from other bodies, for example, volcanism on Io. These materials concentrate and form salt crystals as the ice sublimates. On earth, they are found in dry lake basins (e.g. Devil's Golf Course) where they are formed through a very similar process. The crystalline material can have a wide range of mechanical properties from weak and brittle to hard. Their structures are potentially challenging for surface mobility due to the resulting rugged topology.

### Chaos

There are chaos (Figure 3(e)) regions visible from remote imagery, for example, at Thera Macula on Europa, that display a significant fractured material that is potentially the result of tectonic activity and periodic tidal forces as Europa orbits Jupiter. With cryogenic ice regolith (described in subsection "Cryogenic ice regolith") layered on these chaos regions, the combination of rugged topography and loose granular material will pose significant challenges to mobility and navigation and present a high risk for entrapment.

### Ground material characterization

One of the principal goals of this study was to evaluate the performance of a mobility architecture that has been used on prior planetary exploration missions. Direct measurement of the geotechnical properties of the material on the surface of ocean world bodies is not possible. However, it is possible to physically simulate the material under the expected environmental conditions on these bodies and perform experiments to determine its properties. For wheeled mobility on the surface, the properties of interest are the material shear strength according to the Mohr–Coulomb failure criterion and the bearing strength under normal load. A cryogenic vacuum chamber, capable of maintaining a regolith temperature of 100 K, inside a near-vacuum of 600–1200 Pa as shown in Figure 4, was used to investigate the properties of a granular, cryogenic ice regolith. Measures of these properties enable the estimation of sinkage (a function of bearing capacity) and the thrust (a function of shear strength) that a vehicle may achieve on a granular media. Two particle sizes (10  $\mu\text{m}$  to 2 mm) and two manufacturing processes were used to prepare the ice grain particles for the experiments. The first process, to simulate angular ice grains formed during the fracturing of tectonic processes, was mechanically fractured and sieved directly into a liquid nitrogen bath. The second process, to simulate amorphous particles likely found beside an Enceladus plume, involved liquid water droplets dispersed from an atomizing nozzle directly into a liquid nitrogen bath. The samples did not have any exposure to ambient conditions during these processes to prevent vapor deposition and sintering that would result in

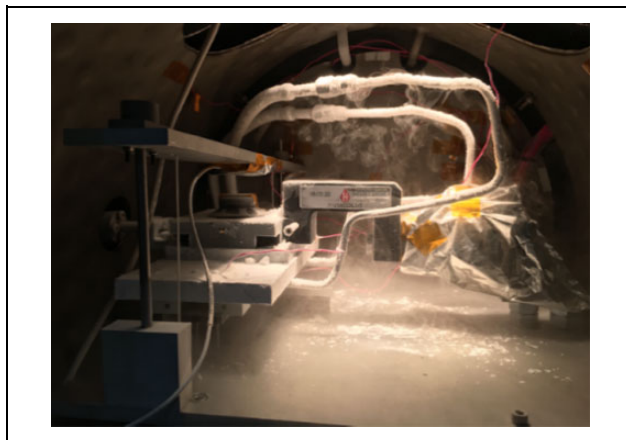


**Figure 4.** Direct shear tests performed on ice regolith in a cryogenic vacuum chamber.

interparticle cohesion. Preliminary results from the direct shear tests are shown in Figure 5. The results from the cryogenic vacuum tests represent one end of the range of terramechanics properties for soils on ocean world bodies where the material is assumed to be composed of loose granular material. The other extreme is for the material to have the properties of hard fused rock.

The significant challenge in developing robotic systems to operate on the extreme planetary surface terrains of Europa and Enceladus is the lack of detailed knowledge of the topography on the scale of the vehicle size and the terramechanics of the material on the surface. That information will remain inaccessible until measurements can be made by future surface missions.

### Vehicle design

To compensate for the lack of information on topography and terramechanics, the design requirements considered in this study are expanded to accommodate a wide range of potential surface geometry and material interaction properties. A similar situation arose in the early 1960s<sup>17</sup> when NASA formulated plans for exploration of our moon prior to the first landing on the surface. The solution developed at the time for surface mobility was the rover developed by General Motors (GM) Defense Research Laboratories<sup>17,18</sup> that could handle very rough, hard terrain while also accommodating weak, noncohesive soils. The GM rover, shown in Figure 6, had a very lightweight chassis with large compliant wheels to distribute its weight and apply minimal ground pressure to *float* on weak soils. It also had a passive suspension system with a flexible chassis to accommodate driving over rough terrain with wheel-height obstacles. Since those early days of vehicle development for planetary exploration, NASA has fielded long-range Lunar Rovers on the moon and Sojourner (shown in Figure 7), Spirit, Opportunity, and Curiosity rocker-bogie suspension rovers on Mars.<sup>19</sup>



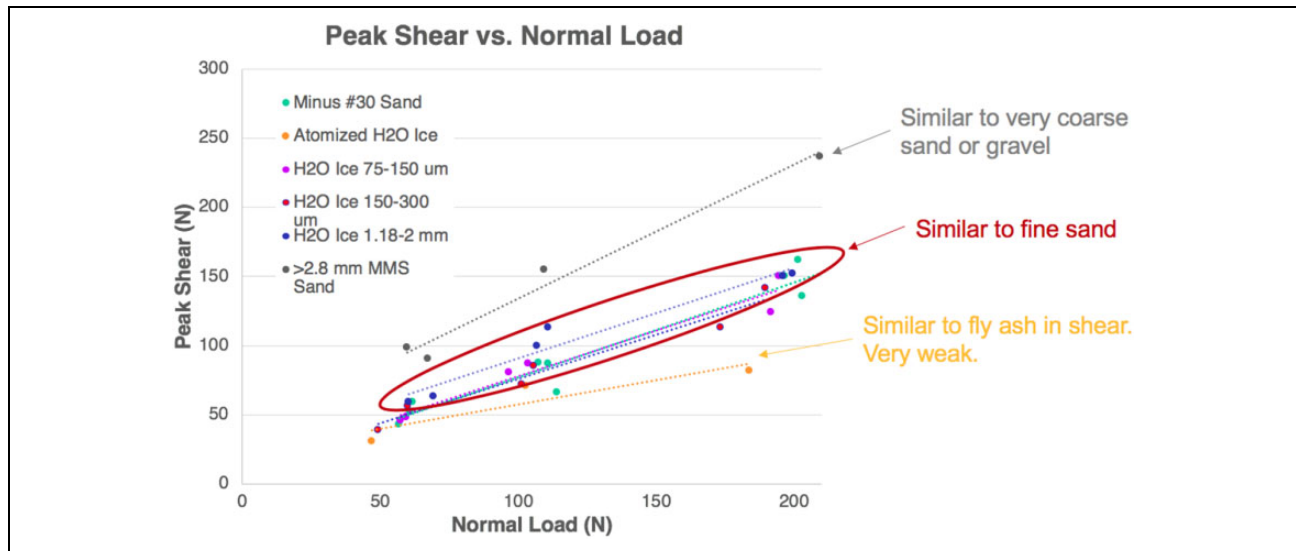


**Figure 5.** Preliminary results from direct shear tests.

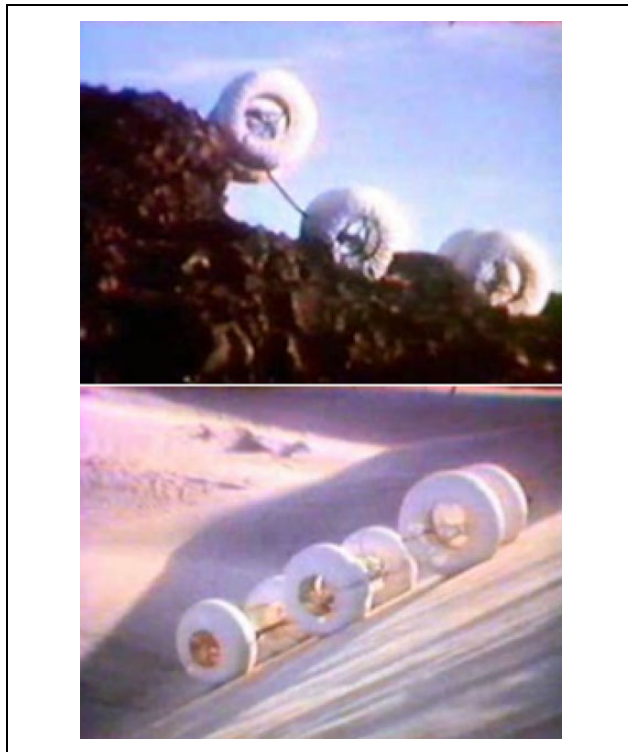


**Figure 6.** This General Motors rover, developed under a contract with NASA, from 1960s was designed to interact with extreme hard terrain (top) and soft soils (bottom). Image credit: Courtesy NASA/JPL-Caltech.

The metrics of performance of vehicles designed for planetary surface exploration are different from terrestrial vehicles.<sup>20</sup> Safety and reliability are of paramount importance. The potentially rugged terrain and low-cohesion soils are the primary challenges for mobility over the surface of ocean worlds. As cryo-vacuum experiments have

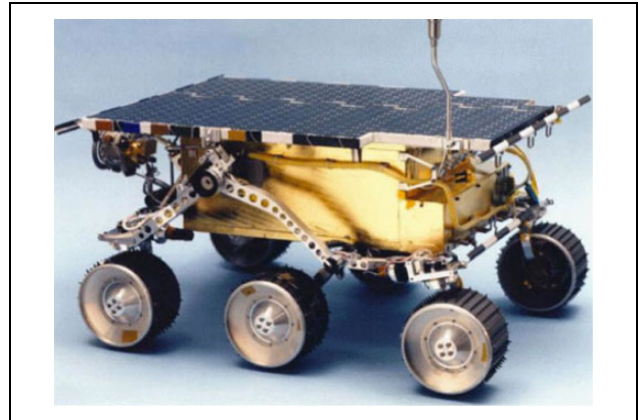


**Figure 7.** Preflight image of Mars Pathfinder rover, Sojourner. Unlike missions on Martian soil, there are no guarantees that rovers can avoid hard terrain with obstacles or low-cohesion soils. Image credit: Courtesy NASA/JPL-Caltech.

confirmed, the Arctic and Antarctic regions on Earth are poor analogs for surface conditions on ocean worlds. The extremely cold surface temperatures on Europa and Enceladus make the conditions very dry. If the material on the surface is fine and granular, it will have low cohesion and its overall behavior may be similar to desert sand.

Many alternative vehicle designs have been proposed for space applications.<sup>21,22</sup> Within the limited resources and time available for this study, the vehicle design solution chosen to address these challenges is to incorporate (1) a large range-of-motion rocker-bogie suspension system to comply to a wide range of topography, (2) large diameter deformable wheels relative to the vehicle size to *float* on soft regolith, and (3) a low center-of-mass for stability. Building on past developments for planetary surface exploration, the design is a hybrid concept that combines

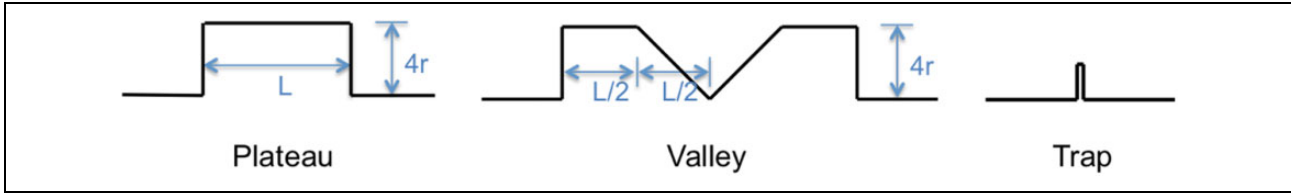


**Figure 8.** Types of terrain geometries considered in this analysis.  $L$  describes the length of the rover from front to back, and  $r$  is the radius of the wheel. The obstacles listed here are an incomplete, but tractably compact set spanning of the types of hard terrain geometries the platforms may interact with.

elements of the GM rover<sup>23,24</sup> and JPL's Mars rocker-bogie suspension rovers.<sup>25–27</sup> Wide and relatively large-diameter wheels are chosen in the design to maintain low ground pressure to address the potential need to handle low-friction soils. Design for handling rugged topography is more involved and an analysis was conducted to select vehicle parameters for the topography. A planar kinematic model of the design with three wheels representing one side of a six-wheeled rover was initially developed, analyzed, and optimized in Matlab.

### Designing through obstacle scenarios

Optimizing mobile platform designs through the lens of worst-case obstacle scenarios can mean designing a platform to be minimally capable of surpassing a specific obstacle. In the past, this criteria has produced rovers built for versatility and long-range mobility. Representative obstacle geometries were selected to capture extremes in topography with twice wheel-diameter-height that the vehicle would need to surmount. For reference, the Rocky 7 rover was designed to overcome obstacles one and a half wheel diameters in size.<sup>28</sup> Here the goal is to minimally achieve locomotion on a class of extreme geometric obstacles (a plateau, valley, and trap) seen in Figure 8. To pass the evaluation, the rover must be able to surpass the obstacles moving both forward and backward. Past work has generated platforms capable of step climbing. One climber is robust to a step gradient,<sup>29</sup> but its capability on other obstacle classes is unclear. Another presents more versatile climbing at the expense of increased mechanical complexity.<sup>30</sup>

Quasi-static force analysis at selected configurations over the obstacles was used in the analysis and the optimization procedure. The objective function was evaluated via the minimum coefficient of friction<sup>31</sup> required to surpass a given obstacle. These kinematic profiles (optimized through static analysis) were then simulated via M3TK to benchmark success on the three obstacles. The optimization procedure determined the kinematic parameters for obstacle climbing and trap avoidance (inability to proceed forward or retreat from an obstacle).

Traction control approaches<sup>32–38</sup> provide the capabilities to increase the effective lower bound of the minimum coefficient of friction. This work uses a simplified

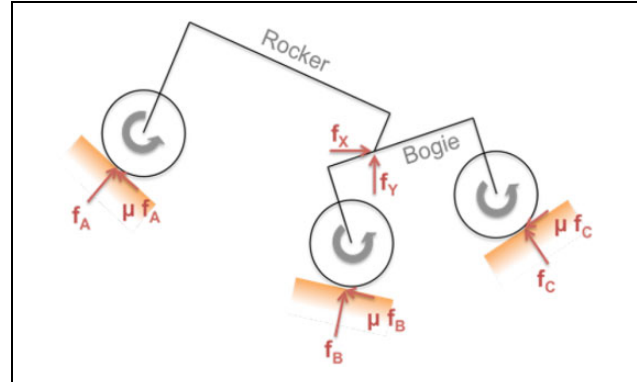


**Figure 9.** Force diagram of a rocker-bogie with wheels (A, B, C ordered rocker side to bogie side) rover located on an uneven terrain. Normal forces  $f_{(A,B,C)}$  are static ground reaction forces exerted by the environment on the rover. Coulomb friction coefficient  $\mu$  determines the magnitude of the orthogonal friction vectors. Hinge joint forces  $f_{(x,y)}$  act perpendicular to and opposite the gravitational field, respectively.

optimization approach by relying simply on static mechanics and a global coefficient of friction shared by all wheels. This places reliability on the static mechanical properties of the system rather than the robustness of the motor control system. Alternative rocker-bogie optimization approaches using an evolutionary algorithm have been used previously<sup>39,40</sup> in simulation environments.

### Design optimization

A 2-D kinematics and static force analysis was used to predict the performance of a parameterized model of a rocker-bogie rover by evaluating the forces and torques at discrete configurations during its traverse over the obstacles. The analysis was further used to find an optimal rover design that maximized performance in being able to traverse over the obstacles with the minimum required friction coefficient. These results were later validated with a full 3-D dynamic simulation of the rover model. The force interactions used in the quasi-static analysis are illustrated in Figure 9. The rover, shown in an arbitrary configuration, needs to balance forces and moments in two dimensions to maintain equilibrium. In the figure,  $(f_x, f_y)$  are the reaction forces at the free rotating hinge between the rocker and the

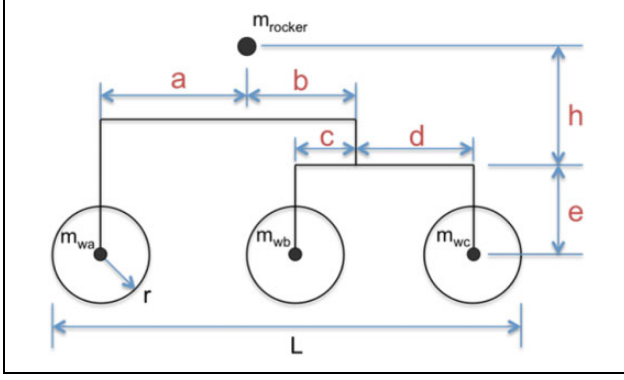


**Figure 10.** Design parameters for the rocker-bogie. Parameters  $r$ ,  $L$ ,  $c$ ,  $d$ , and  $e$  fully constrain the rocker-bogie geometry. Parameters  $h$  and  $(a$  or  $b)$  further distinguish placement of the rocker center of mass  $m_{\text{rocker}}$ .  $L = 1.0$  m and  $r = 0.11$  m inches are constants specified before the optimization.

bogie;  $f_A$ ,  $f_B$ , and  $f_C$  are the normal ground contact forces at the wheels, and  $\mu$  is the Coulomb friction between the terrain and the wheels. The wheel rotation direction, depicted as the gray arrows in Figure 9, determines the direction of the friction forces. Assuming dynamic forces are negligible and the rover is in quasi-static equilibrium as it traverses over the obstacles, the six unknown forces and friction coefficient ( $f_x, f_y, f_A, f_B, f_C, \mu$ ) can be computed from the six equations for force and moment balance of the two rigid bodies, the rocker and the bogie, in (1)

$$\begin{aligned} \sum F_x^{\text{rocker}} &= 0, \sum F_y^{\text{rocker}} = 0, \sum M_z^{\text{rocker}} = 0 \\ \sum F_x^{\text{bogie}} &= 0, \sum F_y^{\text{bogie}} = 0, \sum M_z^{\text{bogie}} = 0 \end{aligned} \quad (1)$$

Inputs to this analysis are the geometry of the rover, the mass of the chassis and wheels, the geometry of the obstacle being traversed (see Figure 10 for all parameters), and the location of the rover along its path of traverse. A mass distribution of the vehicle used in the analysis was chosen to reflect the mass of vehicle components selected for a prototype and is as follows

$$\begin{aligned} m_{\text{rocker}} &= 23\% \text{ of } m_{\text{total}}, m_{w_a} = 23\% \text{ of } m_{\text{total}}, \\ m_{w_b} &= 27\% \text{ of } m_{\text{total}}, \text{ and } m_{w_c} = 27\% \text{ of } m_{\text{total}} \end{aligned}$$

$m_{\text{rocker}}$  is the combined mass of wheel  $w_a$  and the rocker mechanism. The mass of the bogie and wheels  $w_b$  and  $w_c$  are distributed into masses at  $m_{w_b}$  and  $m_{w_c}$ . An analysis based on the condition of the static force equilibrium has long been used in the literature to study obstacle performance of wheeled vehicles theoretically when the rover speed is slow, so the dynamic effect can be ignored. Bekker M and Rettig<sup>41</sup> and Jindra<sup>42</sup> used the static or quasi-static force analysis to study obstacle performance of off-the-road vehicles such as tractors by revealing the relationship between the vehicle design parameters, the obstacle height, and the minimum required friction coefficient to climb over

the obstacle. Siegwart et al.<sup>43</sup> used a quasi-static simulation technique to predict the required friction coefficients for climbing a high vertical step. Kim et al.<sup>29</sup> used a statistical method to find an optimal design of the rocker-bogie mechanism for stair climbing by minimizing the deviation of the center of mass trajectory from a straight line and evaluated the performance of the optimized design using the static force analysis.

In this article, the 2-D quasi-static force analysis was used to predict the performance of a parameterized model of a rocker-bogie rover and was further used to find an optimal rover design that maximizes performance in being able to traverse over the obstacles with the minimum required friction coefficient. The results were validated with a full 3-D dynamic simulation of the rover model. Note that the friction coefficient value is directly used as the cost or objective function in the optimization. The trap avoidance condition, which will be described later, was also incorporated into the optimization to find a design not only with a high performance in climbing but also with a safe driving capability which would be one of the key requirements that enable operating a rover under a harsh circumstance with no human intervention.

In applying the analysis for optimization, the friction coefficient determined from the analysis was used as a metric for the rover's performance. At any configuration, there is a minimum friction coefficient needed to sustain the vehicle in that configuration and be able to apply the force needed to move in the specified direction. For the terrain geometry, the friction coefficient can be computed along the path of the rover as it crosses the terrain. The maximum value of the friction coefficient across the terrain is the minimum needed for the vehicle to completely traverse the terrain.

This *critical friction coefficient* is the minimum needed for the vehicle to traverse the terrain and is a measure of how well the vehicle can traverse terrains with such geometry. It is a function of the rover design parameters (Figure 10) when the geometry of the terrain or obstacle underneath the rover is given. A smaller critical friction coefficient implies better traverse performance. The rover design optimization problem can be decoupled from the material properties of the terrain surface because the *critical friction coefficient* is a purely geometric value that is determined from the rover kinematics and the terrain.

Three simple geometric terrain types, *Plateau*, *Valley* and *Trap*, were used in this analysis to represent and capture the range of challenges to be overcome in traversing ocean worlds terrain. *Plateau* was selected to evaluate the climbing performance of the rover and represent the challenge of surmounting an obstacle. *Valley* was added to capture a different climbing situation where the rover is headed downward and represent the potential to be wedged and the requirement for the vehicle to be able to articulate over concave and convex terrain. The height of these terrains was set to four times the wheel radius. The *Trap*

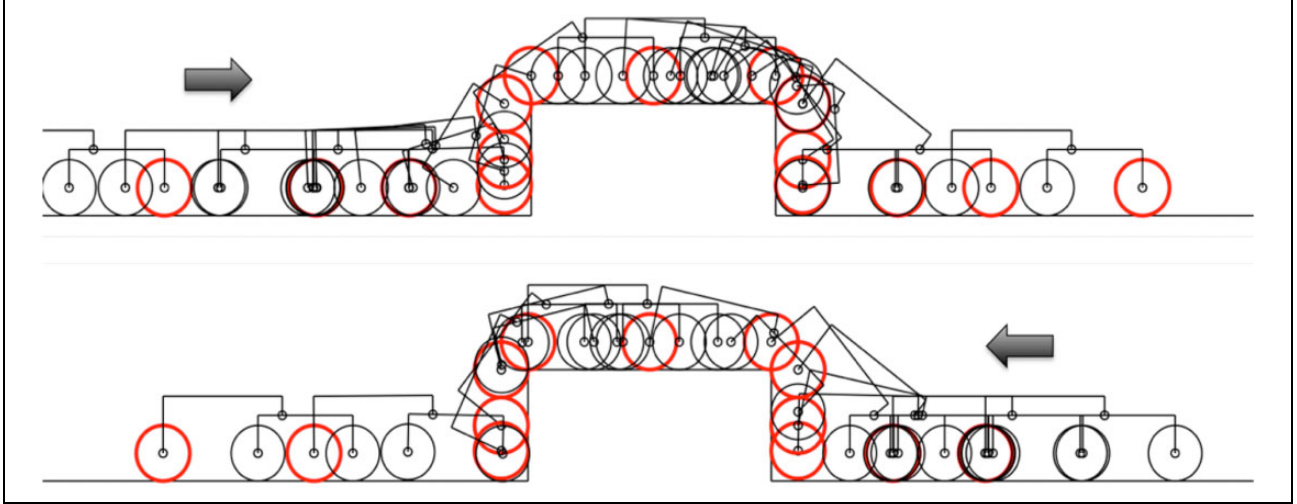


**Figure 11.** An example of sampled rover states on *Plateau* terrain. (The front wheel is colored in red for visual clarity).

terrain (a narrow vertical plane with a height slightly greater than the wheel radius) is used to evaluate the likelihood of the rover to be trapped by obstacles. This is the situation where the front (and possibly middle) wheels of the rover successfully drive over an obstacle but the middle (or possibly rear) wheels are not able to and, furthermore, the rover is not able to reverse out of the situation, that is, the rover drives into a trapped condition that it cannot back out of.

The best kinematic parameters of the rover (Figure 10) to traverse the three terrains were determined through an optimization process. For each terrain type, a simulation of the vehicle traversing over the terrain was generated by sampling the rover state  $s_i$  ( $i = 1, \dots, n$ ) (see Figure 11) and evaluating the corresponding critical friction coefficient at each state,  $\mu_i$ , from a current set of rover design parameters. The maximum value,  $\max(\mu_i)$ , is the critical friction coefficient value that is required for the current rover design to be able to traverse the terrain completely. The optimization process searches the best design in the rover parameter space ( $\mathcal{P}$ ) that minimizes the friction coefficient, that is,

$$\min_{\mathcal{P}} (\max(\mu_i)) \quad (2)$$

In this study, the wheel radius, the drive motor and wheel masses and chassis mass for the control electronics and battery and the total vehicle length were set as fixed values obtained from the hardware components planned for use on the prototype. Only the parameters ( $a, b, c, d, e, h$ ) were treated as the variables to be determined by the optimization. See Table 1 for the fixed parameter values and the constraints between the variables.

The Matlab Optimization Toolbox<sup>44</sup> was used to determine an optimal set of kinematic parameters for the rover over the terrain. More specifically, a Matlab function *fmincon* was used to solve the nonlinear constrained

**Table 1.** Constraints on the parameters.

$r = 0.11$	Wheel radius (m)
$m_{\text{rocker}} = 2.632$	60% of chassis + 2 battery packs (kg)
$m_{wa} = 2.600$	2 wheels + 4 motors (kg)
$m_{wb} = 3.144$	2 wheels + 4 motors + 20% of chassis (kg)
$m_{wa} = 3.144$	2 wheels + 4 motors + 20% of chassis (kg)
$L = 1.00$	Vehicle length (m)
$a + b - c \geq 2r$	Clearance between wheels
$c + d \geq 2r$	Clearance between wheels
$e + h + r \leq 0.5$	Max height of $m_{\text{rocker}}$

optimization problem. The cost function in (2) is highly nonlinear and nonsmooth because of the discrete sampling of the traverse and the iterative solution of the nonlinear equations for the force equilibrium in equation (1). Since the result of the optimization function depends on the initial set of parameters provided, two initial conditions were tried and a better result having a lower cost function value was chosen as the solution. Figure 12 shows the two initial rover designs and the optimized designs found for the three terrain types.

The case of a trap condition is illustrated in Figure 13. The critical friction coefficients of an arbitrarily designed rover is shown at six key states while traversing the terrain with the *Trap*. The rover initially moves to the right in the bogie-facing direction with the critical friction coefficients as shown by the three images in the lower left of Figure 13 then to the left with the critical friction coefficients as shown by the three images in the lower right. In this example, let us assume the actual friction coefficient between the wheels and the terrain is 0.6. For this case, the front wheel is able to drive over the obstacle but the middle wheel is not because it requires a greater friction coefficient (0.82) than is available (0.6). The rover needs to back out to escape from the situation. However, the friction coefficient needed to back out has to be greater than 0.77 (image on the



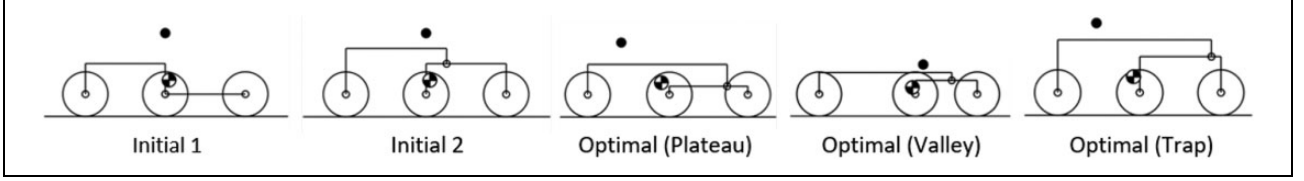


**Figure 12.** Two initial designs and the optimized designs for the three terrain types. ● Centre of mass for rocker and bogie; ● total center of mass (including wheels).

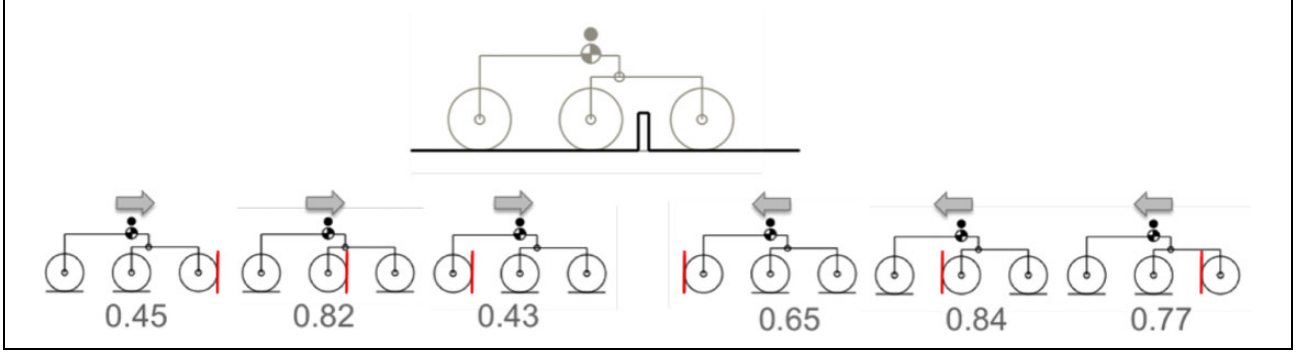


**Figure 13.** For an example rover design, the required friction coefficients ( $\mu$ ) for each wheel to pass the trap obstacle is listed below each six interactions. ● Centre of mass for rocker and bogie; ● total center of mass (including wheels).

furthest right in Figure 12). The vehicle is now trapped with the obstacle between its front and middle wheels. For this case, the first wheel of the rover will not be able to drive over the obstacle in the bogie-facing direction if the wheel-terrain friction coefficient is less than 0.45, it will be trapped if the friction coefficient is between 0.45 and 0.77, and it will be able to drive completely over the obstacle if the friction coefficient is greater than 0.82. However, if driving in the rocker facing direction, because the forward-drive friction coefficients are always greater than the reverse-drive friction coefficients for each wheel, the rover will never find itself in a trapped condition. The condition for not being trapped can be described as the following inequality constraints

$$\mu_1 \geq \mu_2, \mu_1 \geq \mu_3, \mu_4 \geq \mu_5, \mu_4 \geq \mu_6 \quad (3)$$

where  $\mu_i (i = 1, \dots, 6)$  indicate the critical friction coefficients of the six key states from left to right in Figure 12.

The predicted traverse performance of the five rover designs optimized for the *critical friction coefficient* is compared in Figure 14. In Figure 14, the bar graph at the top shows predicted climb performance of the vehicles on the *Plateau* terrain, and the bottom bar graph is for trap-free driving on the *Trap* terrain.

The five rover designs being compared are identified on the horizontal axis. For each design, two bars are shown that represent bogie-facing driving (left-bar) and rocker-facing driving (right-bar). The friction coefficient at the

wheel-terrain contact is shown on the vertical axis. On the bar, green indicate that the friction coefficient is adequate for the vehicle to successfully traverse the terrain. The uncolored area indicates that friction is too low and the vehicle cannot traverse the terrain. For the *Trap* terrain, blue indicates that the vehicle is able to reverse and extricate itself when either its middle or rear wheel cannot overcome the obstacle after the front wheel passes over the obstacle. Red indicates that the rover cannot extricate itself from the situations where an obstacle is either between its front and middle wheels or between its middle and rear wheels.

Not surprisingly, the worst performance in both climbing and trap-free driving and in both driving directions was exhibited by the two initial designs. Also, the design optimized for the *Plateau* terrain, labeled *Optim (Plateau)*, had the best climb performance. The design optimized for the *Trap* terrain, *Optim (Trap)*, also exhibited good climb performance in bogie-facing driving mode, but not as good in rocker-facing driving. Similarly, in Figure 14 (bottom), it can be seen that *Optim (Trap)* has the best trap-condition driving. Overall, the analysis indicates that, of the five designs compared, the *Optim (Trap)* design is almost as good as the *Optim (Plateau)* design in bogie-facing driving and has the least likelihood of being trapped. In rocker-facing driving, however, its climb performance is slightly poorer than the *Optim (Plateau)* design. Given its generally favorable performance, the

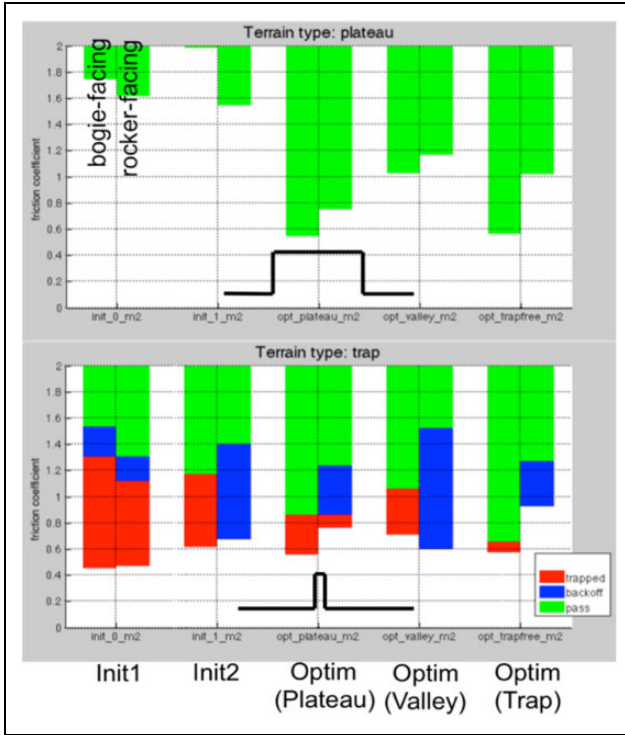


**Figure 14.** Traverse performance of the initial and optimal rover designs predicted on *Plateau* (top) and *Trap* (bottom) terrains. Each column details the success of a given design along a scaling of friction coefficient  $\mu$ . The left and right sides of each column indicate that the bogie and rocker side of the rover (respectively) was led first into the obstacle. No color (white) indicated an inability for the leading wheel to surpass the first ledge of the obstacle. Red indicates that the rover was able to move its first wheel past the leading edge but was unable to disengage. Blue indicates an ability to disengage but an inability to pass through the entire obstacle. Green indicates successful traversal of the obstacle.

*Optim (Trap)* design was chosen as the best design and used in dynamic simulation tests and ultimately for hardware fabrication. The detail parameters from the design optimization are given in Table 2. Numerical values of parameters are indicated in Figure 10.

## Simulation analysis

Following analytical Matlab optimization of the 2-D kinematic rocker-bogie configuration described in section “Design optimization,” full 3-D dynamic simulations of the rover driving over the terrains were performed in M3Tk<sup>45</sup> to further investigate performance that the 2-D optimization analysis might have missed and to validate the model optimization. This approach of verifying performance using dynamics simulators has been pursued by other researchers, for example, to optimize a rhombus-configured, parallel-mechanism suspension rover,<sup>43</sup> to demonstrate the improvements in mobility over rugged terrain using weight distribution control algorithms,<sup>30</sup> to

**Table 2.** Optimized rover design parameters (see Figure 10 for physical locations of the parameters).

Rover configuration	$a$ (m)	$b$ (m)	$c$ (m)	$d$ (m)	$e$ (m)	$h$ (m)
Initial 1	0.39	0	0	0.39	0	0.3
Initial 2	0.39	0.1	0.1	0.29	0.15	0.15
Optimal (Plateau)	0.1632	0.5157	0.2810	0.1011	0.0409	0.2150
Optimal (Valley)	0.5134	0.1411	0.1804	0.1254	0.0682	0.0782
Optimal (Trap)	0.1853	0.5492	0.3422	0.0455	0.1738	0.1615

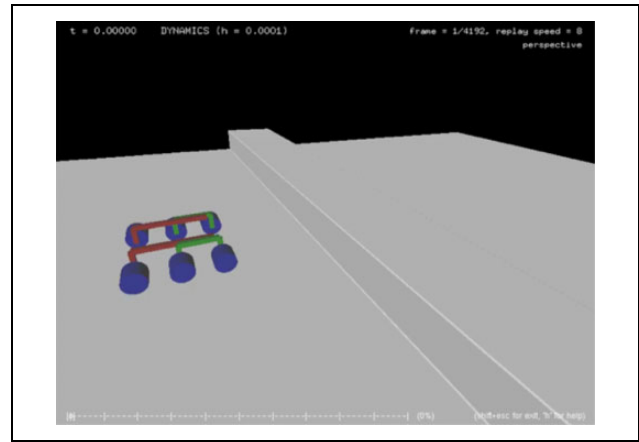


**Figure 15.** A rover model on a terrain in the full 3-D dynamics simulation. In the simulation, the rover was driven over the rectangular barrier to simulate driving over the *Plateau* obstacle.

compare performance of alternative designs of mobility platforms,<sup>31</sup> and to evaluate performance of Mars<sup>46,47</sup> and Lunar<sup>48</sup> rovers.

The parameterization used in the 3-D M3Tk dynamic simulator was identical to that used in the kinematic optimization to allow easy porting of the models directly from the 2-D analysis to the 3-D simulations. The terrain models in the simulation were created using simple geometric cylinder and rectangular prisms (an example is shown in Figure 15) to exactly match the corresponding 2-D model. The collision model for wheel-ground contact used two spheres offset by the wheel width of 0.2 m to represent each wheel. The Kelvin–Voigt contact model<sup>49</sup> was used for wheel-ground normal force calculations with a stiffness of 1,000,000.0 N/m and damping of 800.0 Ns/m, while a linear Coulomb friction model was used for finding tangential forces. During the simulations, wheel velocities were controlled to a constant angular velocity of 0.5 rad/s. All simulation runs were straight-line drives that did not require steering.

The first step in developing stable 3-D simulations was to determine suitable parameters for the ground contact model, gains for the wheel actuator controllers for stable vehicle operation and maintaining acceptable and constant

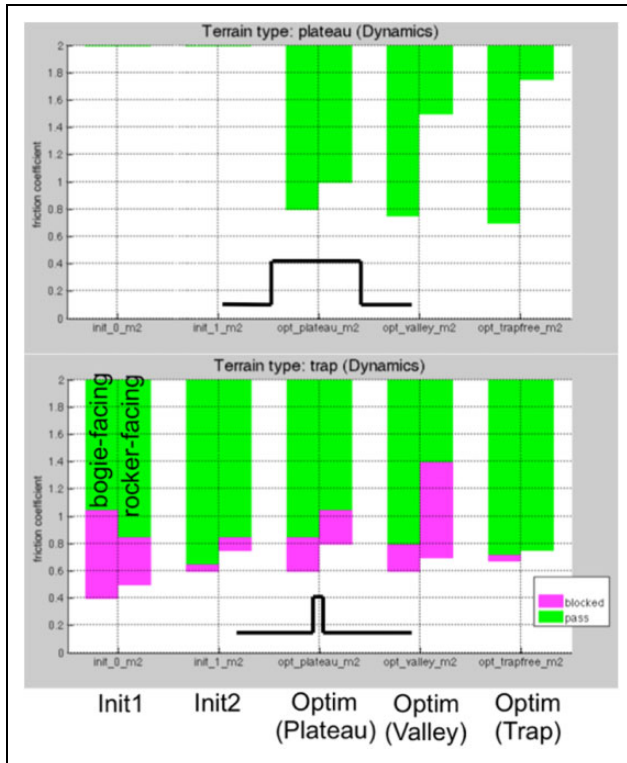


**Figure 16.** Comparison of obstacle performance for candidate rover designs in the full 3-D simulator. Bar graph conventions are consistent with Figure 14, with the exception of a magenta region, which includes both trapped and back off scenarios.

vehicle velocities. To compare performance against the design optimization analysis, a series of simulations were then run with the identical trap, plateau, and valley terrain models. Multiple simulation runs were conducted over these terrains with ground contact friction varied from 0.05 to 1.3 in increments of 0.05. Results for the minimum required friction coefficient for traversal of the obstacles were generated using this approach so they could be directly compared to the optimization analysis results. Simulation runs included evaluating the trap conditions where one or two wheels would not be able to traverse over the trap.

The results from the 3-D simulations were consistent with the results of the 2-D kinematic optimization analysis. As before, the two initial designs turned out to have very poor traverse performance. As was found in the design optimization analysis in section “Design optimization,” the 3-D simulations showed the *Optim (Trap)* design had the best trap-free driving performance and good performance over the plateau and valley terrains. In simulating the trap condition, backing out of a trapped situation was not implemented. Instead, if trapped, the simulation run was marked as *blocked* and shown in magenta in Figure 16. Therefore, the magenta color indicates situations that include *trapped* and *back-off* conditions shown in red and blue in Figure 14. Comparing the results from the design optimization in Figure 14 and the 3-D simulations in Figure 16, we see that,

although not identical, the qualitative trends are similar and they validate each other.

The 3-D dynamics simulations showed two issues with the rover design. The first issue was the potential for the rover to flip over onto its back when attempting to climb over the front vertical wall of the traverse obstacle for the *Plateau* and *Valley* obstacles. The flip would occur when the two front wheels were at the top of the obstacle and the rear wheels were still on the ground. In this configuration, the center of mass of the rocker–bogie would migrate to be behind the rear wheels due to the height of the obstacle, causing the unsupported weight to destabilize the vehicle and flip it over. The application of a higher fidelity mass distribution, with mass of the wheels and accounting for the steer and drive motors in the wheels, lowered the center of mass of the vehicle, increased stability, and solved the flip-over problem. The design optimization described in the previous section was also updated with the more accurate mass distribution.

The second issue found from the simulations was that the vehicle had a tendency to do a *wheelie* when driving with the rocker in the front. This behavior has been observed in the Mars rover vehicles.<sup>50</sup>

The *wheelie* behavior occurred when the rocker front wheels contacted the obstacle and slip. The rear wheels continued to drive the rocker–bogie suspension mechanism forward laterally squeezing the mechanism and causing the middle wheels to lift off the ground. The consequent reduction in total vehicle traction force with only the front wheels contributing traction (rear wheel traction is expended rotating the rocker–bogie suspension and the middle wheels are off the ground) further reduced the normal forces that the front wheels could apply to the obstacle to generate traction to surmount the obstacle. In the 3-D simulation, an algorithm for traction control was implemented to stop driving the rear wheels as soon as the middle wheels lifted off the ground. With this solution, traction was maintained and enabled the vehicle to climb the obstacle. An extension of this algorithm that controlled velocity ratios of the wheels was implemented and successfully demonstrated in the prototype that was developed later in this effort.

Given an optimal vehicle kinematic configuration, it is possible to improve the performance of the vehicle using traction control algorithms. This can be achieved, for example, by controlling the center of mass and the load distribution on the wheels<sup>32</sup> or applying wheel torque based on the anticipated traction load from a geometric analysis of the vehicle configuration and the terrain profile<sup>33,34</sup> as was recently implemented on the Mars Science Laboratory Curiosity rover.<sup>51</sup>

## Wheel grouser analysis and design

The previous section inspected the relationship between platform design parameters and required frictional contact

to surpass various terrain types. Varying the geometry of grousers has a substantial effect on the contact mechanics when interacting with granular and hardened terrains. Prior research<sup>52</sup> developed a grouser spacing equation through experimental studies in loose granular soil. Here, it was identified that a small number of grousers could introduce resistive flows of loose soil, reducing tractive efficiency. This work also noted that large diameter and compliant wheels may be less susceptible to forward soil flow, reducing the tractive efficiency dependence on a high grouser count. For ocean worlds mobility, the existence of cryogenic ice, penitentes, salt evaporites, and chaotic terrains (Figure 3 (a), (b), (d), and (e)) warrants further analysis of grousers designed for hardened and geometrically uncertain terrains. The experiments and analysis in this section will motivate parametrizations of grousers that maximize safety on hard terrains (critical to mission goals). Further tests optimizer grouser design for mobile efficiency and energetic efficiency on rough terrain. The latter two are noncritical to mission goals but remain valuable as softer guides in the development and testing of ocean worlds rover prototypes.

### Grouser design space

The Mars 2020 Rover team has performed extensive analysis and testing of rover wheels.<sup>53</sup> These grouser shapes included sinusoidal, diagonal, and other geometric patterns. Testing concluded that a straight grouser (cleat contours run parallel to the wheel axel) was the most predictable and robust to extreme terrains. Variations within the space of straight grousers are what will be considered for implementation on the ocean worlds platforms. The wheels on the rover will be approximately 61 cm in diameter and 15.2 cm in width, with grousers extending from this exterior geometry. Figure 17 illustrates the resulting design space, grouser height ( $h$ ), grouser thickness ( $t$ ), and number of grousers ( $n = 2 * \pi / \theta$ ). In this analysis, grousers were modeled as spanning the width of the wheel.

A Matlab script was written to generate geometric CAD models of the wheels from parametrized inputs ( $h$ ,  $t$ ,  $n$ ). A program was written to generate the mesh inputs for this variation of geometric compositions. Candidates considered existed within the design space, as shown in Table 3.

### Ledge climbing

By testing on a variation of terrain geometries, the design candidates can be filtered from consideration. In the first part of the grouser analysis, ledge climbing simulations help to determine a range of parameters adept for handling hard terrain obstacles.

A grouser's ability to lift a wheel off the ground and latch onto elevated terrain is key for performance on potentially hard, uneven surfaces. In this simulation, each grouser encounters a sequence of ledges with increasing height

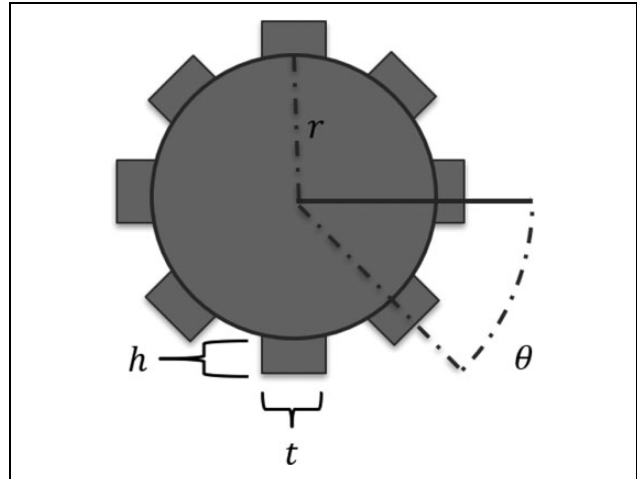


**Figure 17.** Grouser design parameters include the height  $h$ , thickness  $t$ , and number of grousers  $n$ , where  $n$  is related to the grouser pitch  $\theta$  by  $n = 2\pi/\theta$ . The wheel's outer radius is of fixed length  $r = 30$  cm.

**Table 3.** Range of parameter values for grouser design.

Parameter	Lower bound	Upper bound
Grouser height, $h$ (cm)	0	15.2
Grouser thickness, $t$ (rad)	0.035	0.105
Number of grousers, $n$	1	36

(2.5 cm per new ledge). Its performance is indicated by the highest ledge it crests. Each straight ledge protrudes normal to the flat ground surface, as shown in Figure 18. Nine hundred wheel candidates were tested containing from 1 to 36 grousers and spanning 0 cm to 15.2 cm height (0.6 cm intervals). Grouser thickness within the bounds specified in the table was deemed to have a negligible impact on the ability to climb. Each grouser in this simulation had a thickness of 0.087 rad.

The graph in Figure 18 distinguishes the grouser designs that can reliably navigate sharp changes in terrain elevation. The regions of the design space with critical mobility concerns are explained below.

Designs on the leftmost part of the diagram in Figure 18 struggle due to a lack of reach provided by the short grousers. The reach of the grouser to the ledge is restricted and compounded by the lack of vertical lift generated on the wheel from the short grouser on the bottom. Increasing the grouser height will generally allow for higher ledge traversal. Mobility also requires structural integrity, energy efficiency, and various traction considerations. The grouser height will remain restricted to under  $r/2$ , one quarter of the wheel diameter. On the bottom of the diagram, climbing issues result from not having enough grousers. In this case, it is less likely that grouser lift on the bottom will be paired with grouser latch on the top. This can be seen in the two-grouser configuration in Figure 19(a).



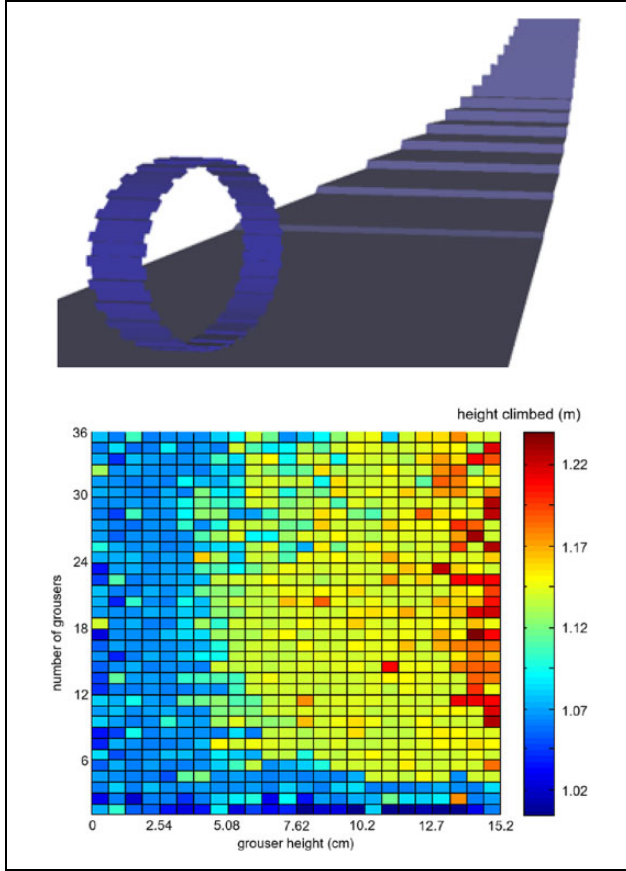


**Figure 18.** In the edge climbing simulation, each wheel candidate attempts to climb the series of ledges of increasing height. Each ledge is perpendicular to the ground. The height climbed metric details the maximum height of an individual ledge climbed by the wheel. Low-performance grouser designs (blue and green regions) were caused by (1) short grousers, (2) not enough grousers, or (3) too many grousers.

Configurations on the top part of the diagram in Figure 18 can be impeded by the tight spacing of many grousers. The normal force of a lower grouser against the vertical face of an edge will prevent an upper grouser from successfully latching on. For mechanical intuition, one might think of a high number of grousers as acting like a wheel. At  $\lim_{n \rightarrow \infty}$ , the wheel simply adds a radius of length  $h$  and receives no latching benefit from the grouser. This effect can be seen in Figure 19(b).

From this analysis, the following recommendations are made on grouser parameters to minimize interaction with issues detailed above when climbing terrain obstacles:

- grouser height should be greater than  $r/12$  wheel diameter
- use between 8 and 28 grousers.

Using more than 28 grousers may be standard for short grouser passing through a regolith. These suggestions are meant to enhance capabilities when interacting with the extreme, hard geometric obstacles of ocean worlds.

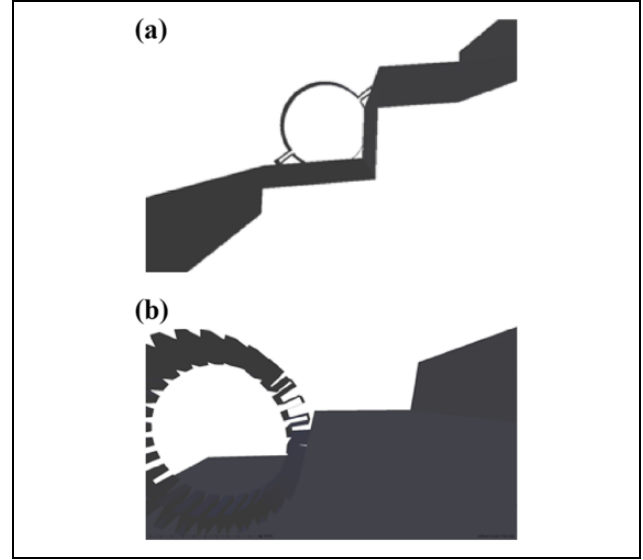


**Figure 19.** A two grouser configuration (a) fails to grasp the ledge, it receives no lift from the  $\pi/2$  offset grouser. On the right (b), a high number of grousers fail to grasp the ledge. Ascending a ledge is identical geometrically to climbing the front end of a plateau. Maximal ledge heights climbed are recorded in Figure 18.

Through this simulation, a conservative filter of the grouser design space is taken. Wheels in subsequent simulations will have between 3 and 36 grousers from 2.5 cm to 15.2 cm thick, and the filter can be seen in the box in Figure 18.

### Mobility testing of grousers

Here, the analytical focus shifts from recommending safe configurations for grousers to testing the mobile efficiency of grousers on randomized terrains.

*Individual wheel on smooth and rough terrains.* In this section, a smaller subset of designs in the number of grousers and height space are tested while experimenting with varied grouser thicknesses. The design space is the following: 1368 wheel candidates were tested containing from 3 to 36 grousers (sampled in increments of 3) and spanning 2.5 to 15 cm in height (2.5 cm intervals). Grouser thickness spanned  $2^\circ$  to  $6^\circ$  with quarter degree increments. Grousers below 2.5 cm ( $r/12$ ) in height and 3 in numbers of grousers were filtered from future testing by the ledge climbing tests.

Each wheel, still held by a massless 2-D gantry, is free to move in one plane. Over a 20-s trial, the wheels are evaluated on how far they can locomote, given a prescribed angular velocity of 1 rad/s. The wheels move slowly to ensure that difference in performance is determined by shape relationship between the wheel and terrain rather than the dynamic properties of either. Smooth and rough terrains are generated by starting with a flat terrain mesh and displacing the vertices of this mesh vertically by small

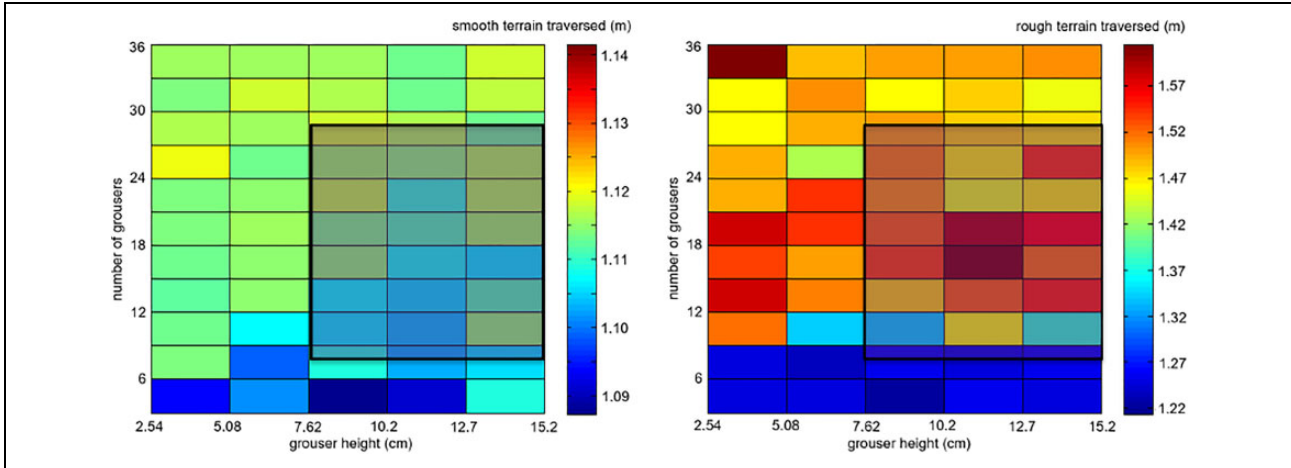


**Figure 20.** A 2-D gantry restricts wheels to planar motion over randomized terrain. The left and right plots show thickness-averaged performance across smooth and rough terrains, respectively. The shaded region indicates a region which traveled the farthest along the terrain in a 20-s trial.

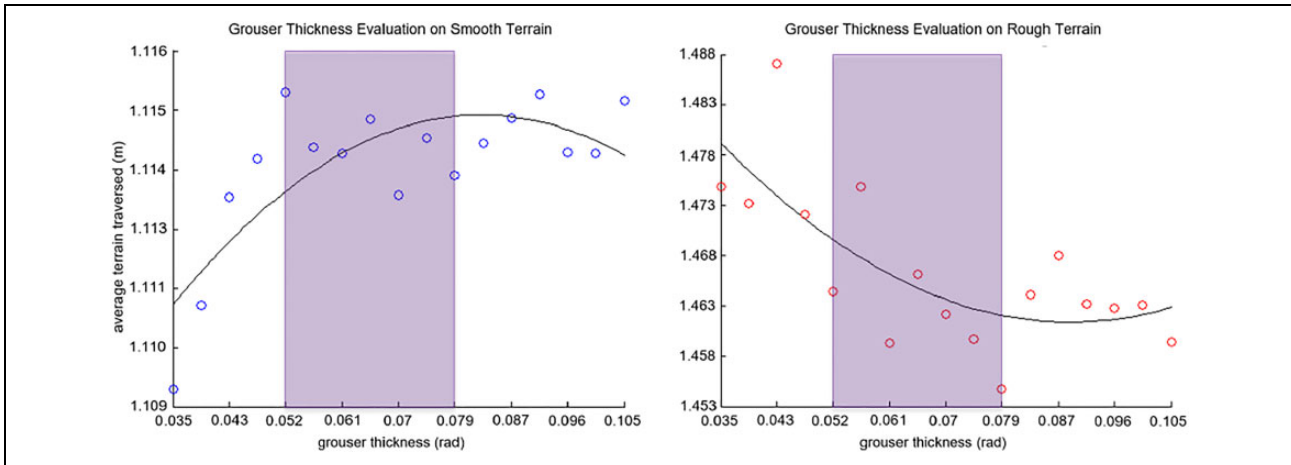


**Figure 21.** From the same experiments shown in Figure 20, this plot shows two different relationships between grouser thickness and length of terrain traversed during simulation. On smooth terrain, thicker grousers convert more normal force to force that propels the rover forward. Thinner grousers, as hinted at in Figure 19, allow for a larger spatial window for latching onto variations in the terrain and propelling the platform forward.

perturbations (smooth terrain) and large perturbations (rough terrain). The perturbations are driven by white noise of various scales. Figure 20 shows that the wheels travel quite farther on the rough terrain, which suggests that the accelerating force generated from gripping a jagged portion of the terrain is larger than that experienced by the normal force multiplied by the coefficient of friction on the smooth terrain.

In Figure 21, grouser thickness is plotted from the same experiment set shown in Figure 20. On smooth terrain, it is preferable to have a large surface area in contact with the terrain, thus a preference for larger thickness is shown. On rough terrain, thinner grousers enable more spacing to hook on to jagged parts of the terrain, accelerating it forward. From these data, an interval of  $3^\circ$  to  $4.5^\circ$  is selected as ideal

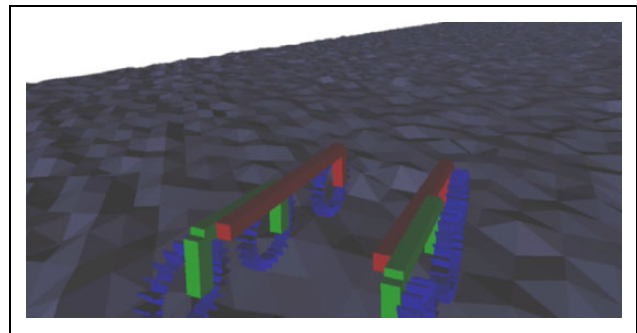


**Figure 22.** Each wheel-grouser configuration is equipped on a rocker-bogie and tested across smooth and rough terrain. Randomized terrains are generated via stochastic perturbation of mesh points that are initially evenly distributed in a plane orthogonal to gravity.

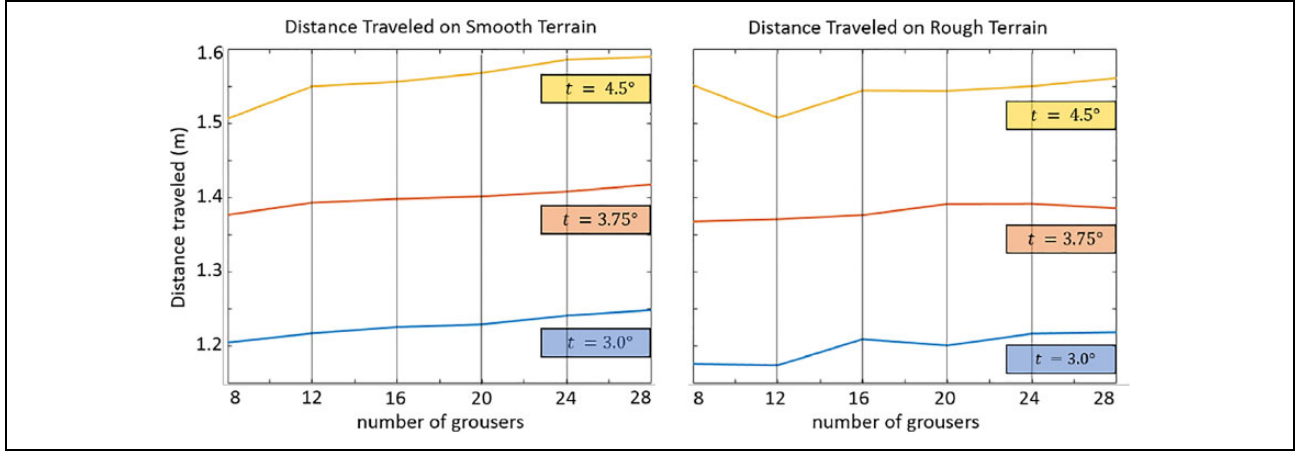


**Figure 23.** Grouser thickness (primarily) and the number of grousers contribute to the overall mobility of the rocker–bogie in terms of distance traveled on randomized terrain (per timed simulation).

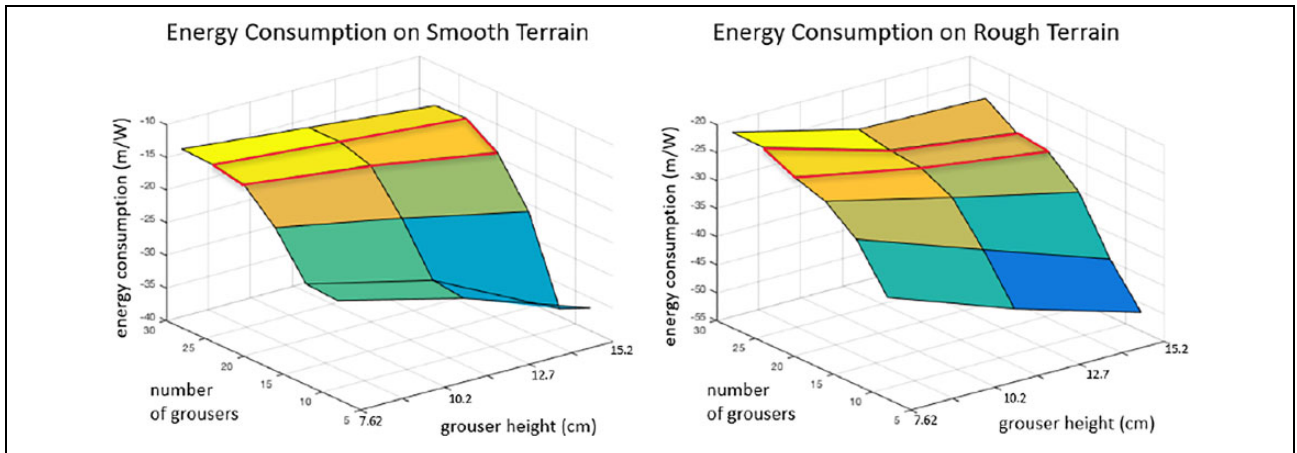


**Figure 24.** This graph shows rocker–bogie energy consumption for a variety of wheel configurations on smooth (left) and rough (right) terrains. For low numbers of grousers, energy efficiency scales very poorly with grouser height.

for each situation. This is comparative to the grouser thickness commonly observed on rovers.

**Rocker–bogie on rough terrains.** A smaller subset of the more exhaustive tests above will be simulated with a rocker–bogie. The 54 design configurations tested span the following parametrizations:

- $h = [7.62 \text{ cm}, 11.43 \text{ cm}, 15.2 \text{ cm}]$
- $t = [0.0524 \text{ rad}, 0.0655 \text{ rad}, 0.0785 \text{ rad}]$
- $n = [8, 12, 16, 20, 24, 28]$

To evaluate performance of each simulation, the path length accumulated along a 20-s simulation on the hard terrains is tracked. In Figure 23, it appears the thickness can have a big impact on long-range mobility of these platforms. Furthermore, the number of grousers is positively related to the range traveled, but with a less substantial impact.

### Energy efficiency of grousers

The grousers are also tested for energy efficiency in Figure 24. It is shown for more than 20 grousers on a given wheel, efficiency scales very well with grouser height. Energy is computed by multiplying torque and angular distance. When a small number of grousers are present, the impact of each cleat contacting the ground appears to draw a higher torque from the wheel motors to maintain the 1 rad/s angular velocity. For high numbers of grousers, this impact is mitigated, partially due to the decreased space between contact points on the wheel. This tends to draw a lower torque upon impact of an individual grouser. Taking into account energetic and mobility concerns, the number of grousers suggested for the platform design is between 20 and 24. In Figure 25, one can see a visualization of highest performing grouser designs for efficiency testing. However, the primary goal for this analysis is to enable the navigation

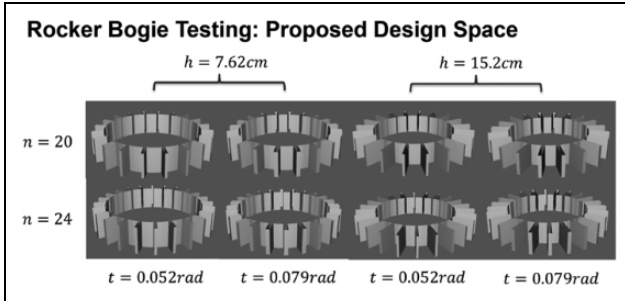


**Figure 25.** These wheels presented span the highest performing on efficiency tests over hard terrain. As the parametrization in Figure 17 indicates, the diameter is fixed. The 15 cm grouser images are scaled down in the figure.

of hard geometric obstacles. The criteria for good ledge climbing will be used as a stricter guide in the testing of grouser prototypes.

## Experimental evaluation

### Prototype development

A fully functional six-steer-and-drive-wheel hardware prototype vehicle was built to the specifications from the kinematic optimization and dynamic simulation analysis. The prototype was designed to be structurally reconfigurable in order to experimentally determine performance as a function of various kinematic parameters. The design was composed of modular parts connected structurally using tubular links that could be adjusted in length. A key component in the design were the six identical wheel-steer assemblies. Commercial off-the-shelf compliant wheels were chosen as a baseline component which were then modified as prescribed by the grouser optimization analysis. The mechanical design of the grousers for the rover was experimentally iterated through several options on material and geometric properties. The final design used a thread with grousers that was 3-D printed from a compliant material and fitted over the wheel. For added traction and wear resistance, spikes were embedded in the outside edges of the grousers.

For the prototype, a wheel drive module was designed to fit inside the wheel hub. It was connected to the steer module through a cantilevered tubular link that aligned the steer axis through the center of the wheel as shown in Figure 26. Optical encoders were used to sense the wheel drive velocities. For sensing wheel steer angles, absolute magnetic encoders were used.

On each side of the rover chassis, a rocker joint and a bogie joint were connected to each other and the three steer-drive wheel assemblies using the tubular links. Adjustable hard stops were designed into these joints to allow for parametric evaluation of the effect of joint limits on the mobility of the vehicle. The left- and right-side suspension assemblies were connected to each other with a crossbeam tube through the rocker joints. The left and right rockers are



**Figure 26.** Wheel steer assembly for a scaled down prototype rocker-bogie. The design was built to the kinematics of the optimized rocker-bogie in sections “Design optimization” and “Simulation analysis” within the grouser design constraints of section “Ledge climbing.”

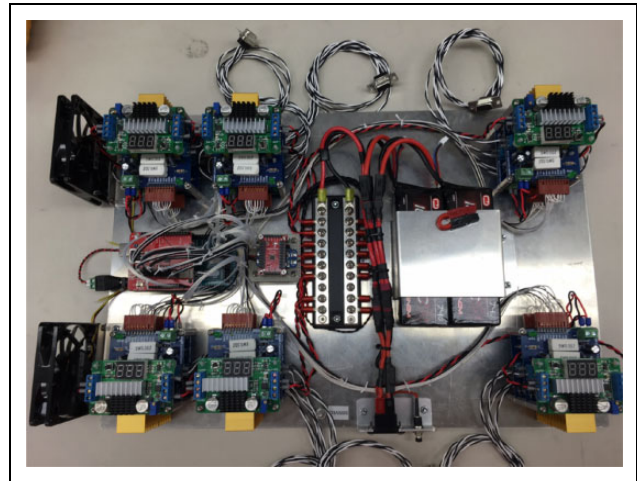


**Figure 27.** Rover on-board electronics system.

constrained to rotate in equal and opposite amounts via a mechanical linkage, which is also reconfigurable. This constraint reduces the degrees of freedom of the suspension to three, which passively constrains all six wheels to the ground.

A drive electronics box was designed to house the power, communication, computing, and motor controller elements for the rover. The contents of the box are shown in Figure 27. An Atmel Mega 2560 microprocessor implemented the onboard algorithms for safety, power management, wireless communication, and driving. Software was also implemented on the microcontroller to facilitate debugging and data logging. Twelve H-bridge motor controller boards were used to drive the twelve motors and monitor motor currents. The electronics box and its





**Figure 28.** Prototype rover driving over a rock at a test yard at JPL.

contents were driven by two enclosed lithium-ion polymer batteries.

Teleoperated driving was implemented using a radio-controlled joystick. Drive algorithms implemented included straight-line, arc, and crabbing velocity modes. On-board software translated the 2-D drive commands into wheel steer angles and drive velocities based on the Ackerman steering algorithm.<sup>54</sup> The wheel steer values computed were sent to the PID steering motor controller. The drive motors were controlled open loop by setting desired motor rotation rates. Steer PID control parameters were experimentally tuned for optimal performance. The prototype was extensively driven at an outdoor facility and performed well in varied terrain including soft and loose granular soils as well as over rocks. Figure 28 shows the assembled vehicle in field operations.

## Evaluation

To evaluate the performance of the rover prototype in comparison to the simulation predictions, accurately sized physical mock-up models of the *Plateau* and *Valley* terrain types were built. Performance over the *Trap* terrain condition was not evaluated because the rover design chosen was optimized for that terrain condition. The terrain mock-ups were constructed of 2.5-cm-thick plywood sheets and coated with paint with embedded grit to simulate realistic terrain. The static friction coefficient of the surface was measured to be 0.61 and the dynamic coefficient was 0.54.

Experimental evaluations were performed by manually commanding the rover using the joystick input device to drive over these terrain mock-ups to replicate the configurations and scenarios analyzed in section “Design optimization” and the motions simulated in section “Simulation analysis.” Figure 29 shows the rover driving over the *Plateau* and *Valley* terrain mock-ups.

The experimental procedure was to place the rover a few centimeters from and aligned with the respective mock-up.

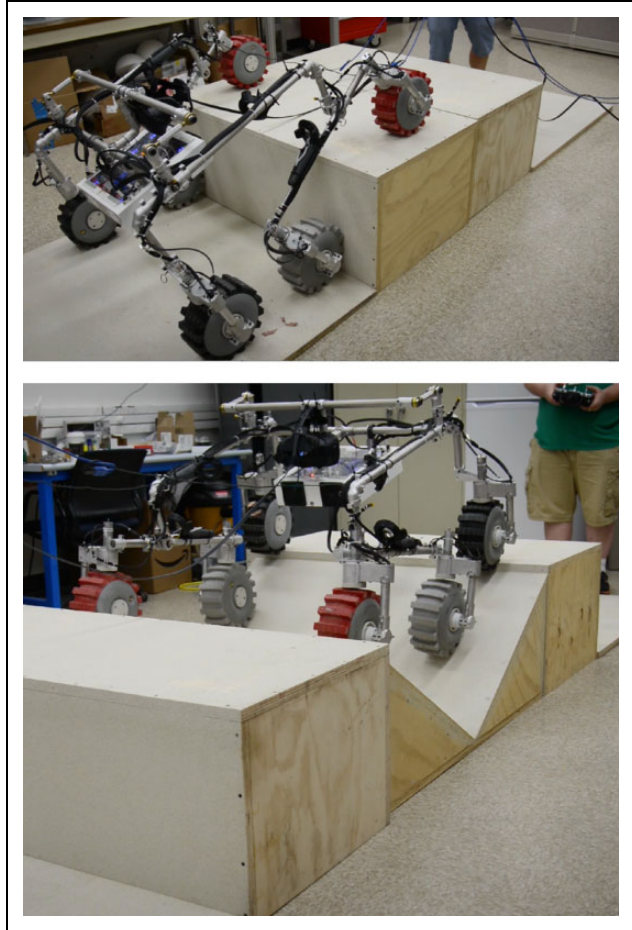


**Figure 29.** Experiment set up for *Plateau* (top) and *Valley* (bottom) driving.

The rover was then commanded to drive forward to approach and climb over the mock-up until it completed the maneuver and its back wheels were past the trailing edge of the terrain mock-up. This was repeated four times for the *Plateau* and *Valley* mock-ups. During the experiments, a motion capture system was used to independently track the positions of the rover chassis and the left and right rocker and bogie positions. The data logged from the motion capture system are compared to data logged from the dynamics simulation runs to validate the design process and confirm the performance of the prototype.

The experimental and simulation data generally correlate well (see Figures 30 and 31 for representative examples of the results). The discrepancies are primarily due to calibration errors in the motion capture system and differences between the physical experimental terrain set-up and the simulation terrain. However, the overall objective of using rigorous analytical optimization combined with a high-fidelity simulation to design a vehicle is generally borne out in the success of the prototype in negotiating the challenging *Plateau* and *Valley* terrain obstacles. The goal of developing a rover capable of climbing a vertical obstacle

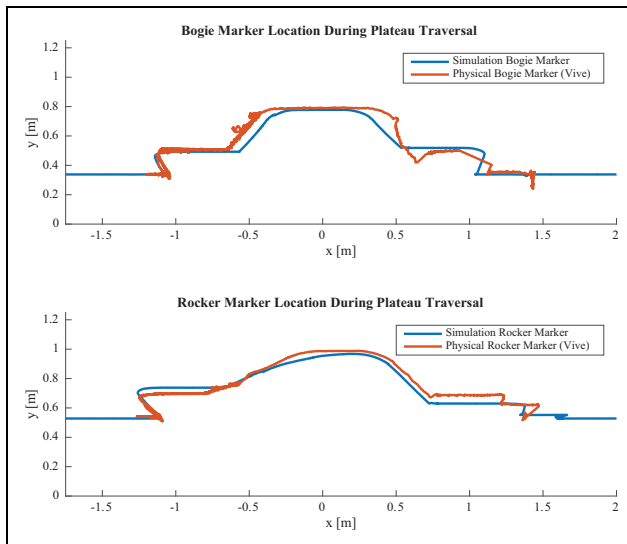


**Figure 30.** Comparison of bogie (top) and rocker (bottom) results from simulation and experiment for *Plateau* terrain.

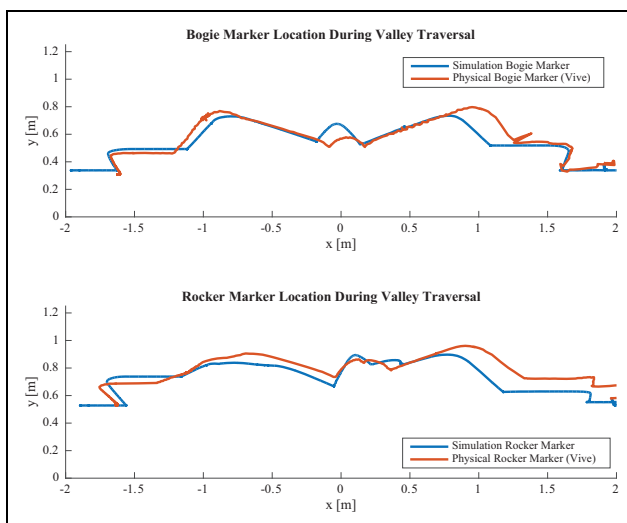


**Figure 31.** Comparison of bogie (top) and rocker (bottom) results from simulation and experiment for *Valley* terrain.

two times its wheel diameter by optimizing the kinematics and mass distribution of the vehicle was successful.

## Conclusions

This investigation studied the surface environmental conditions on ocean world bodies and designed and developed a prototype vehicle to be able to traverse its surface. The prototype was evaluated using physical mock-ups of challenging analog terrain features. Evaluation results have shown that its performance correlates well with the kinematic and dynamic analysis, it is able to surmount obstacles two-times wheel diameter in height, and performs better

when in the bogie-facing drive configuration. The overall approach pursued of using analytical and simulation tools to design the vehicle was found to be successful. To perform long-range surface exploration to address geology and origins science goals on ocean world bodies, a vehicle with comparable capabilities will be needed.

The appeal of missions to ocean worlds has increased as more becomes known about their environmental conditions. Technology for surface exploration will have to be developed to achieve the desired science goals on these bodies while meeting the environmental constraints and mission requirements. This study developed a concept vehicle, demonstrated it in simulation, and evaluated its performance in experiments to show that it will be capable of mobility over varied ocean worlds terrain. Two potential upcoming Europa missions, an orbiter and a lander, will provide significantly more information of the surface of Europa, reduce the uncertainty, and provide mobility system engineers with more specific requirements to design against.

## Authors' note

The research described in this publication was carried out at the Jet Propulsion Laboratory of California Institute of Technology under contract from the National Aeronautics and Space Administration. Portions of the work reported in this article were previously presented. This article provides greater depth and includes new and unpublished results from experiments on a prototype and an analysis and design of the wheel.

## Acknowledgment

The authors gratefully thank the reviewers for their constructive suggestions.


## Declaration of conflicting interests

The authors declared no potential conflicts of interest with respect to the research, authorship, and/or publication of this article.

## Funding

The author(s) disclosed receipt of the following financial support for the research, authorship, and/or publication of this article: The work was funded by NASA as is stated in the Author's Note above. I don't understand the reason for this statement. This seems to be an incorrect statement.

## ORCID iD

Hari Nayar  <https://orcid.org/0000-0001-5484-2797>

## References

1. Porco CC, Helfenstein P, Thomas PC, et al. Cassini observes the active south pole of Enceladus. *Science* 2006; 311(5766): 1393–1401.
2. Kivelson MG, Khurana KK, Russell CT, et al. Galileo magnetometer measurements: a stronger case for a subsurface ocean at Europa. *Science* 2000; 289(5483): 1340–1343.

3. Franck S, Block A, Bloh WV, et al. Habitable zone for Earth-like planets in the solar system. *Planet Space Sci* 2000; 48(11): 1099–1105.
4. Sykes MV. The Future of Solar System Exploration (2003–2013)–Community Contributions to the NRC Solar System Exploration Decadal Survey. In: *The Future of Solar System Exploration (2003–2013)–First Decadal Study contributions*. Vol. 272. California: Astronomical Society of the Pacific, 2002.
5. Kattenhorn SA and Hurford T. Tectonics of Europa. *Europa*. 2009, pp. 199–236.
6. Nayar H, Kim J, Meirion-Griffith G, et al. Surface mobility on ocean worlds. In: *Aerospace conference*, Big Sky, MT, 2017, pp. 1–10. IEEE.
7. Spencer JR, Tamppari LK, Martin TZ, et al. Temperatures on Europa from Galileo photopolarimeter-radiometer: nighttime thermal anomalies. *Science* 1999; 284(5419): 1514–1516.
8. Brown RH, Clark RN, Buratti BJ, et al. Composition and physical properties of Enceladus' surface. *Science* 2006; 311(5766): 1425–1428.
9. Paranicas C, Cooper J, Garrett H, et al. Europa's radiation environment and its effects on the surface. *Europa* 2009; 529.
10. Sparks W, Hand K, McGrath M, et al. Probing for evidence of plumes on Europa with HST/STIS. *Astrophysical J* 2016; 829(2): 121.
11. Wu X and Prakash V. Dynamic compressive behavior of ice at cryogenic temperatures. *Cold Reg Sci Technol* 2015; 118: 1–13.
12. Hobley D, Moore J, and Howard A. How Rough is the Surface of Europa at Lander Scale? In: *44th Lunar planetary science conference*, The Woodlands, TX, 2013, p. 2432.
13. Moore JM, Black G, Buratti B, et al. Surface properties, regolith, and landscape degradation. In: Pappalardo RT, McKinnon WB, and Khurana K (eds.) *Europa*. Tucson : University of Arizona Press, 2009, pp. 329–349.
14. Buratti BJ, Nelson RM, and Lane AL. Surficial textures of the Galilean satellites. *Nature* 1988; 333(6169): 148–151.
15. Nelson RM, Boryta MD, Hapke BW, et al. Laboratory simulations of planetary surfaces: understanding regolith physical properties from remote photopolarimetric observations. *Icarus* 2018; 302: 483–498.
16. Nelson RM, Boryta MD, Hapke BW, et al. Jupiter's Satellite Europa: evidence for an extremely fine-grained, high porosity surface. In: *AAS/Division for Planetary Sciences Meeting Abstracts* 2015; 47.
17. De Fries P. Lunar surface locomotion. *Adv Space Sci Technol* 1967; 9: 275.
18. Asnani V, Delap D, and Creager C. The development of wheels for the Lunar Roving Vehicle. *J Terramechanics* 2009; 46(3): 89–103.
19. Bickler D. Roving over mars. *Mech Engine* 1998; 120(4): 74.
20. Wong JY. *Theory of ground vehicles*. Hoboken: John Wiley & Sons, 2008.
21. Seeni A, Schafer B, Rebele B, et al. Robot mobility concepts for extraterrestrial surface exploration. In: *Aerospace conference*, 2008, pp. 1–14. Piscataway: IEEE.
22. Bruzzone L and Quaglia G. Locomotion systems for ground mobile robots in unstructured environments. *Mech Sci* 2012; 3(2): 49–62.
23. Bekker MG. Mechanics of locomotion and lunar surface vehicle concepts. *SAE Transactions* 1964; 72: 549–569.
24. Pavlics F. Interview with Ferenc Pavlics. Sam Romano, Don Freidman and Nick DiNapoli, Santa Barbara, CA. 2007.
25. Harrington BD and Voorhees C. The challenges of designing the rocker-bogie suspension for the mars exploration rover. *JPL Technical Report* 2004.
26. Lindemann RA and Voorhees CJ. Mars exploration rover mobility assembly design, test and performance. In: *IEEE international conference on systems, man and cybernetics*, Vol. 1, Waikoloa, HI, 2005, pp. 450–455. IEEE.
27. Welch R, Limonadi D, and Manning R. Systems engineering the Curiosity rover: a retrospective. In: *8th international conference on system of systems engineering (SoSE)*, Maui, HI, 2013, pp. 70–75. IEEE.
28. Hayati S, Volpe R, Backes P, et al. The Rocky 7 rover: a Mars sciencecraft prototype. In: *Proceedings – IEEE international conference on robotics and automation*, 1997, Vol. 3, Albuquerque, NM, 1997, pp. 2458–2464, IEEE.
29. Kim D, Hong H, Kim HS, et al. Optimal design and kinetic analysis of a stair-climbing mobile robot with rocker-bogie mechanism. *Mech Mach Theory* 2012; 50: 90–108.
30. Skonieczny K and D'Eleuterio GM. Improving mobile robot step-climbing capabilities with center-of-gravity control. In: *ASME 2010 international design engineering technical conferences and computers and information in engineering conference*. Am Society Mech Engine 2010; pp. 1531–1538.
31. Thueer T, Krebs A, Siegwart R, et al. Performance comparison of rough-terrain robots—simulation and hardware. *J Field Robotics* 2007; 24(3): 251–271.
32. Sreenivasan S and Wilcox B. Stability and traction control of an actively actuated micro-rover. *J Robotic Syst* 1994; 11(6): 487–502.
33. Iagnemma K and Dubowsky S. Traction control of wheeled robotic vehicles in rough terrain with application to planetary rovers. *Int J Robot Res* 2004; 23(10-11): 1029–1040.
34. Lamon P, Krebs A, Lauria M, et al. Wheel torque control for a rough terrain rover. In: *IEEE international conference on robotics and automation (ICRA 2004)*, 2004. IEEE: ETH-Zurich.
35. Toupet O, Biesiadecki J, Rankin A, et al. Traction control design and integration onboard the mars science laboratory curiosity rover. In: *2018 IEEE aerospace conference*, Big Sky, MT, 2018, pp. 1–20. IEEE.
36. Grand C, Benamar F, Plumet F, et al. Stability and traction optimization of a reconfigurable wheel-legged robot. *Int J Robotics Res* 2004; 23(10-11): 1041–1058.
37. Chen G, Zhang WG, and Zhang XN. Speed tracking control of a vehicle robot driver system using multiple sliding surface control schemes. *Inter J Adv Robotic Sys* 2013; 10(2): 90.

38. Albagul A and Wahyudi. Dynamic modelling and adaptive traction control for mobile robots. *Inter J Adv Robotic Sys* 2004; 1(3): 16.
39. Seeni A, Schafer B, and Hirzinger G. Conceptual rover design by an integrated optimization process. In: *International symposium on artificial intelligence, robotics and automation in space*, Sapporo, Japan, 2010.
40. Leite AC and Schäfer B. Planetary Rover Optimization Tool (ROT). In: *Proceedings of the XV International Symposium on Dynamic Problems of Mechanics, MA Savi (Editor), ABCM, Buzios, RJ, Brazil, February, 2013*, pp. 17–22.
41. Bekker M and Rettig G. *Obstacle performance of wheeled vehicles. Land Locomotion Laboratory, US Army Ordnance Tank-Automotive Command, Report* 1958.
42. Jindra F. Obstacle performance of articulated wheeled vehicles. *J Terramechanics* 1966; 3(2): 39–56.
43. Siegwart R, Lamon P, Estier T, et al. Innovative design for wheeled locomotion in rough terrain. *Robot Auton Syst* 2002; 40: 151–162.
44. Branch MA and Grace A. MATLAB: optimization toolbox: user's guide version 1.5. *The MathWorks*; 1996.
45. Mukherjee R, Myint S, Chang J, et al. Robot mobility and manipulation modeling toolkit. In: *ASME 2014 international design engineering technical conferences and computers and information in engineering conference. American Society of Mechanical Engineers* 2014; pp. V007T05A003–V007T05A003.
46. Yen J, Jain A, and Balaram J. ROAMS: Rover analysis, modeling and simulation software. *JPL Technical Report* 1999.
47. Jain A, Balaram J, Cameron J, et al. Recent developments in the ROAMS planetary rover simulation environment. In: *2004 IEEE aerospace conference proceedings (IEEE Cat. No. 04TH8720)*, Vol. 2, Big Sky, MT, 2004, pp. 861–876. IEEE.
48. Nayar H, Balaram BJ, Cameron J, et al. A Lunar surface operations simulator. In: *International conference on simulation, modeling, and programming for autonomous robots*, Venice, Italy, 2008, pp. 65–74. Springer.
49. Meyers MA and Chawla KK. *Mechanical behavior of materials*. Vol. 2. Cambridge: Cambridge University Press, 2009.
50. Bickler D. The Mars rover mobility system. *JPL Technical Report*, 1997.
51. Toupet O, Biesiadecki J, Rankin A, et al. Traction control on the curiosity mars rover: algorithm and flight results. *Journal of Field Robotics (submitted)* 2019.
52. Skonieczny K, Moreland SJ, and Wettergreen DS. A grouser spacing equation for determining appropriate geometry of planetary rover wheels. In: *IEEE/RSJ international conference on intelligent robots and systems (IROS)*, Vilamoura, Portugal, 2012, pp. 5065–5070. IEEE.
53. Arvidson R, DeGrosse P, Grotzinger J, et al. Relating geologic units and mobility system kinematics contributing to Curiosity wheel damage at Gale Crater, Mars. *Journal of Terramechanics* 2017; 73: 73–93.
54. Volpe R. Inverse kinematics for all-wheel steered rovers. *Internal Jet Propulsion Laboratory Memo* 1999.